PERGAMON

Journal of the Mechanics and Physics of Solids
49 (2001) 1823–1846

JOURNAL OF THE
MECHANICS AND
PHYSICS OF SOLIDS

www.elsevier.com/locate/jmps

Thermomechanical response of AL-6XN stainless steel over a wide range of strain rates and temperatures

Sia Nemat-Nasser[a,*], Wei-Guo Guo[a], David P. Kihl[b]

[a] *Center of Excellence for Advanced Materials, Department of Mechanical and Aerospace Engineering, University of California, San Diego, La Jolla, CA 92093-0416, USA*
[b] *Naval Surface Warfare Center, Carderock Division, Bethesda, MD 20084, USA*

Received 4 January 2000; accepted 9 August 2000

Abstract

To understand and model the thermomechanical response of AL-6XN stainless steel, uniaxial compression tests are performed on cylindrical samples, using an Instron servohydraulic testing machine and UCSD's enhanced Hopkinson technique. True strains exceeding 40% are achieved in these tests, over the range of strain rates from 0.001/s to about 8000/s, and at initial temperatures from 77 to 1000 K. In an effort to understand the underlying deformation mechanisms, some interrupted tests involving temperature and low- and high-strain rates, are also performed. The microstructure of the undeformed and deformed samples is observed by optical microscopy. The experimental results show: (1) AL-6XN stainless steel displays good ductility (strain $> 40\%$) at low temperatures and high-strain rates, with its ductility increasing with temperature; (2) at high-strain rates and 77 K initial temperature, adiabatic shearbands develop at strains exceeding about 40%, and the sample breaks, while at low-strain rates and 77 K, axial microcracks develop at strains close to 50% or greater; (3) dynamic strain aging occurs at temperatures between 500 and 1000 K and at a strain rate of 0.001/s, with the peak value of the stress occurring at about 800 K, and becoming more pronounced with increasing strain and less pronounced with increasing strain rate; and (4) the microstructure of this material evolves with temperature, but is not very sensitive to the changes in the strain rate. Finally, based on the mechanism of dislocation motion, paralleled with a systematic experimental investigation, a physically based model is developed for the deformation behavior of this material, including the effect of viscous drag on the motion of dislocations, but excluding the dynamic strain aging effects. The model predictions are compared with the results of the experiments. Good agreement between the theoretical predictions and experimental results is obtained. In order to verify the model independently of the experiments used in the modeling, additional compression tests at a strain rate of 8000/s and various initial

*Corresponding author. Tel.: +1-838-534-4914; fax: +1-838-534-2727.
E-mail address: sia@halebopp-uesd.edu (S. Nemat-Nasser).

PII: S0022-5096(00)00069-7

temperatures, are performed, and the results are compared with the model predictions. Good correlation is observed.

Keywords: AL-6XN; Strain rate; Aging; A. Microstructure; Modeling

1. Introduction

AL-6XN is a relatively new nitrogen-strengthened austenitic stainless steel. Austenitic stainless steels are usually noted for their high strength and exceptional toughness, ductility, and formability. They exhibit considerably better corrosion resistance than martensitic or ferritic steels and also have excellent strength and oxidation resistance at elevated temperatures. The key difference between AL-6XN and other austenitic stainless steels, such as Nitronic 50 (22-13-5), is that AL-6XN contains more nickel and molybdenum. It is known that, higher nickel contents improve the chloride SCC (stress–corrosion cracking) resistance, whereas molybdenum and nitrogen provide improved pitting and crevice corrosion resistance (Brooks and Lippold, 1990), since alloys high in nickel content can display improved austenite stability (Denhard and Espy, 1972). Because of its similarity with Nitronic 50 (Gaugh and Perry, 1972), this very special austenitic stainless steel, AL-6XN, is also expected to have the following properties:

1. Resistance to intergranular attack, superior to that of Types 304L and 306L stainless steels, when sensitized; and approximately twice the 0.2% yield strength of Types 304 and 316, while maintaining excellent ductility and toughness.
2. Higher elevated-temperature strength than the standard 300 series stainless steels.

It is known that austenitic stainless steels exhibit a single-phase, face-centered cubic (fcc) structure that is maintained over a wide range of temperatures. This structure results from a balance of alloying additions that stabilize the austenite phase from elevated to cryogenic temperatures. Because these alloys are predominantly single phase, these materials attain an increased strength through solid–solution hardening rather than by age-hardening (they are not hardenable by heat treatment). Therefore, they retain their full strength even when welded in heavy sections. They can be used in the as-welded condition without loss of strength or impaired corrosion resistance.

Several studies have addressed the strain-rate and temperature effects on the strength of austenitic stainless steels (Ishikawa and Tanimura, 1992; Hecker et al., 1982; Stout and Follansbee, 1986). However, the plastic deformation of AL-6XN at low to high temperatures and over a wide range of strain rates, has received relatively little attention, mainly because of the relatively recent origin of the material. The present paper addresses two major objectives. First, in order to examine the plastic flow of AL-6XN and the corresponding deformation mechanisms, systematic compression experiments are performed at low- to high-strain rates and over a wide range of temperatures, and the microstructure of the deformed samples is examined by an optical microscope. Second, using the experimental results, and based on the mechanisms of thermally activated dislocation motion, the drag-controlled effects, and the farfield resistance to dislocation movements, a physically based model is developed for this material and

Table 1
Major alloy content of AL-6XN (%)

C	Cr	Ni	Si	Mn	Mo	N	Cu
0.024	20.56	23.84	0.36	0.41	6.21	0.213	0.20

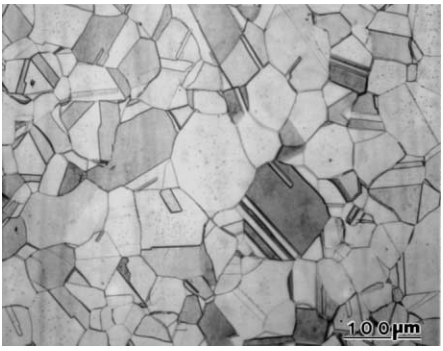

Fig. 1. Microstructure of AL-6XN material.

its predictive capability is experimentally verified by independent tests. The model, however, does not include the effect of the dynamic strain aging which is observed at low-strain rates over the temperature range of 500–1000 K.

2. Experimental procedure and results

2.1. Material and samples

All tests are carried out on an AL-6XN baseplate. The chemical composition of this stainless-steel baseplate is show in Table 1.

To minimize the presence of residual stress, all samples are fabricated by EDM (electro-discharge machining). They have a 3.8 mm nominal diameter and 3.8 mm height. To reduce the end friction on the samples during the low- and high-strain deformation, the sample ends are first polished using waterproof silicon carbide paper, 1200 and 4000 grid, and then they are greased for low- and room-temperature tests. A molybdenum-powder lubricant is used for the high-temperature experiments. It is known that the austenitic stainless steels exhibit good oxidation resistance at elevated temperatures up to nearly 600°C (Brooks and Lippold, 1990). Therefore, no special atmosphere is needed below this temperature. To examine the microstructure of the undeformed and deformed samples, the samples are sectioned along the loading direction, then polished and etched, as required by standard metallography. The etching reagent is the Aqua regia: 15 ml HCI and 5 ml HNO_3. Fig. 1 shows the microstructure of an undeformed sample. The average grain size in this figure is about 40 μm.

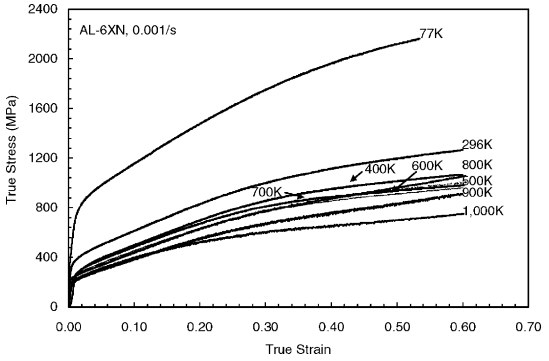

Fig. 2. True stress–true strain curves for indicated temperatures and a strain rate of 0.001/s.

Twins are observed in this initial material, possibly due to pre-thermal–mechanical treatment.

2.2. Low and high strain-rate tests

Compression tests at strain rates of 0.001/s and 0.1/s are preformed using an Instron hydraulic testing machine, over a wide range of temperatures from 77–1000 K, with true strains exceeding about 60%. Elevated temperatures are attained with a high-intensity quartz-lamp, radiant-heating furnace in an argon environment (in the present work, an argon atmosphere is used for temperatures exceeding 800 K). The temperature is measured using a thermocouple arrangement. The temperature is maintained constant to within $\pm 2^{\circ}$C. The deformation of the specimen is measured by LVDT, mounted in the testing machine, and is calibrated and compared with the results of a standard extensometer before the test. The low temperature of 77 K is obtained by immersing the specimen and the testing fixture in a bath of liquid nitrogen. Typical true stress–true strain curves of AL-6XN at strain rates of 0.001/s and 0.1/s are displayed in Figs. 2 and 3, respectively.

Dynamic tests at strain rates of 1000/s and 3500/s are performed using UCSD's recovery Hopkinson technique (Nemat-Nasser et al., 1991; Nemat-Nasser and Isaacs, 1996) at temperatures of 77 to 1000 K, and strains exceeding 40%. For the high-strain-rate tests at elevated temperatures, it is necessary to heat the sample to the required temperature while keeping the incident and transmission bars of the Hopkinson device at a suitably low temperature. To do this, Nemat-Nasser and Isaacs (1996) have developed a novel enhancement of the compression recovery Hopkinson technique (Nemat-Nasser et al., 1991) for high-temperature tests, where a furnace is employed to preheat the specimen, while keeping the transmission and incident bars outside the furnace. These bars are then automatically brought into gentle contact with the specimen, just before the stress pulse reaches the specimen-end of the incident bar. The temperature is measured by a thermocouple which also holds the specimen inside the furnace.

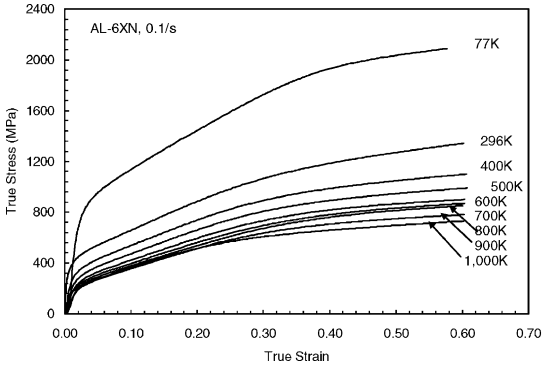

Fig. 3. True stress–true strain curves for indicated temperatures and a strain rate of 0.1/s.

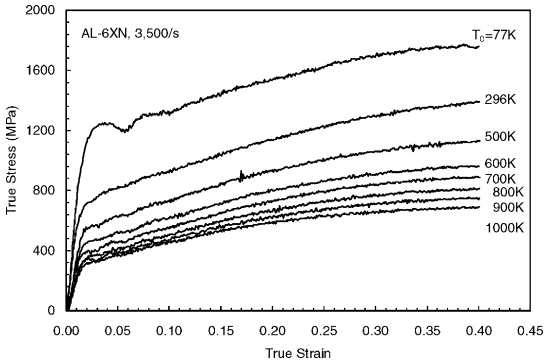

Fig. 4. Adiabatic stress–strain curves for indicated initial temperatures and a strain rate of 3500/s.

The true stress–true strain curves at a strain rate of 3500/s are shown in Fig. 4. UCSD's recovery Hopkinson technique makes it possible to obtain an isothermal flow stress at high-strain rates and various temperatures. The isothermal flow stress of AL-6XN at a strain rate of 3500/s and temperatures of 77–500 K, is given in Fig. 5.

2.3. Experimental results and discussion

2.3.1. Microstructure

2.3.1.1. Low- and room-temperature results. Samples display visible shear failure when tested at a strain rate of 3500/s and at an initial temperature of 77 K, to true strains exceeding 60% (adiabatic). The true stress–true strain curve for a typical case is given in Fig. 6 (marked 3500/s (adiabatic)). As seen, the stress attains a peak value at about 40% strain, then it drops with increasing strain, as shearbands form and the sample fails. Fig. 7 shows the profile of a shear fracture, occurring at an angle of 45° to the loading direction (the loading direction in all subsequent micrographs is the same as that in Fig. 7).

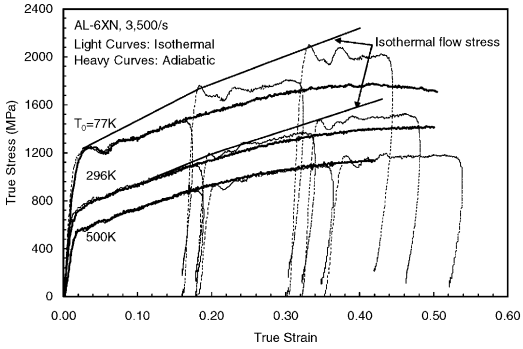

Fig. 5. Comparison between adiabatic and isothermal flow stress at 3500/s.

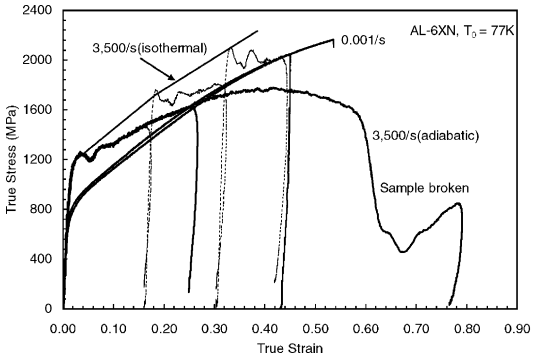

Fig. 6. True stress–true strain curves for 0.001/s and 3500/s at the same 77 K temperature; only pre-peak data are meaningful.

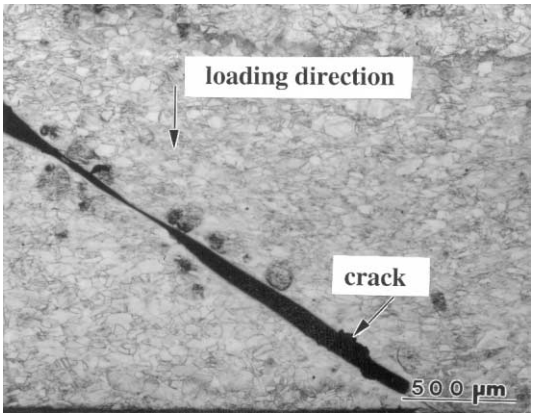

Fig. 7. Adiabatic fracture strained to $\gamma = 56\%$ at 77 K initial temperature and 3500/s.

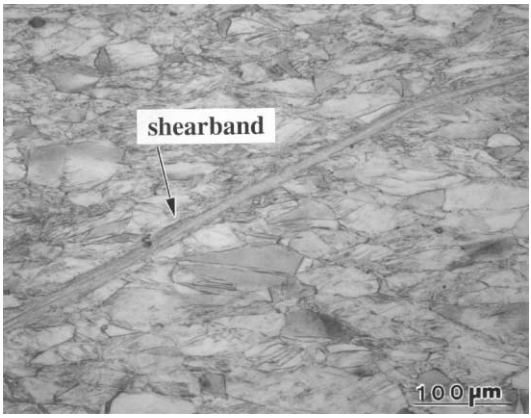

Fig. 8. Adiabatic shearband in a sample strained to $\gamma = 70\%$ at 296 K initial temperature and 3500/s strain rate.

In general, as adiabatic shearbands develop, the stress in the sample begins to drop from a maximum value. To check this, an interrupted test at a fixed initial temperature and a fixed strain rate, is performed, to a strain of about 25%. The corresponding true stress–true strain curve is shown in Fig. 6 (this curve falls on the adiabatic curve of 3500/s). No shearband is noticed in the corresponding micrograph. Similarly, no shearbands are seen to form when the sample is tested incrementally to about 42%, at a 3500/s strain rate, in order to develop the isothermal true stress–true strain curve shown in Fig. 6 (marked 3500/s (isothermal)). On the other hand, pronounced shearbands occur when a sample is deformed to about 70% strain, at a 3500/s strain rate, starting with the initial room temperature (296 K); see Fig. 8. As seen, there are no voids or cracks within or outside the shearband in this figure. The peak stress in this case occurs at about 55% strain. It thus appears that, at high-strain rates, shearbands can develop in this material, as the test temperature is decreased to 77 K, or when the true strain exceeds 40%.

It is generally agreed that adiabatic shearbands are triggered by local inhomogeneities such as geometric or dimensional variations, temperature differences, and perhaps the presence of voids or inclusions (Merzer, 1982; Wu and Freund, 1984; Liao and Duffy, 1998). From Figs. 4 to 6, it is seen that the AL-6XN stainless steel has high strength at the low temperature of 77 K. If the sample is loaded at a 77 K initial temperature and a 3500/s strain rate, its temperature can reach about 310 K at a true strain of 60%. Since the material has a low thermal conductivity, at high-strain-rate deformations, the heat produced by plastic deformation cannot rapidly be dispersed, leading to failure by adiabatic shearbanding. The isothermal tests at the same high-strain rate to the same final strain, on the other hand, do not lead to shearbanding and, hence, do not cause failure.

When the sample is strained to 54% at a strain rate of 0.001/s and at 77 K, a microcrack is seen to develop along the loading direction. This microcrack is about 0.23 mm in length, occurring close to the loading surface.

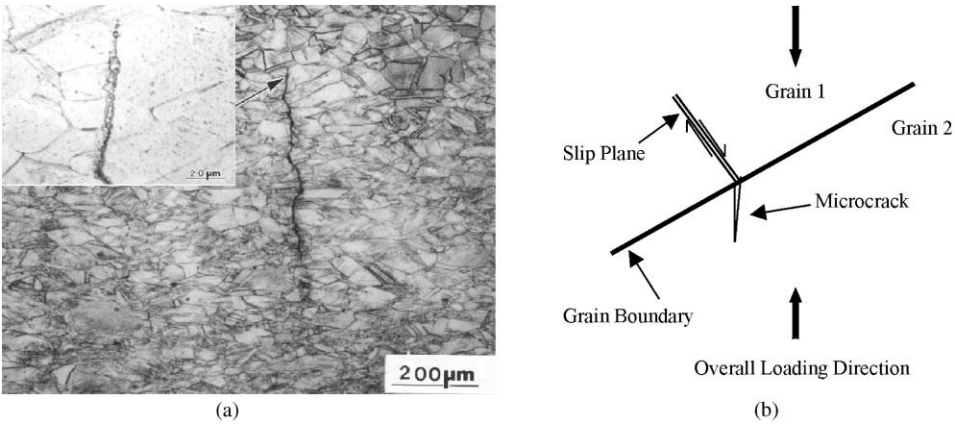

Fig. 9. (a). Microstructure of a sample strained to $\gamma = 80\%$ at 296 K and 0.001/s. (b). A microcrack may form under compression, in an unfavorably oriented crystal when a slip plane intersects the grain boundary.

To check this further, the microstructure of another sample which is strained to about 44% at 77 K (mark 0.001/s in Fig. 6) is examined, revealing no microcracks. On the other hand, a sample strained to about 80% at a 0.001/s strain rate and at 296 K, develops a microcrack of about 0.44 mm, as is seen in Fig. 9a. This figure also shows that the microcrack encompasses a number of small grains. At the higher strain rate of 0.1/s, we observe no microcracks in a sample strained to 60% at 77 K, nor in a sample strained to 70% at 296 K.

Microcracking in the direction of axial compression is typically observed in brittle failure, and is referred to as "axial splitting" (see Nemat-Nasser and Horii, 1982; Horii and Nemat-Nasser, 1985, 1986). Cracks of this kind are produced by local defects which can create a local tension, although the overall applied stress is compression. For example, when a slip plane of a crystal intersects another unfavorably oriented crystal in a polycrystalline solid, a microcrack may be nucleated (see Fig. 9b).

2.3.1.2. Microstructure at high temperature. Fig. 10 shows the microstructure of a sample strained to 80% at a strain rate of 0.001/s and a temperature of 1000 K. We have also examined the microstructure of this material tested at temperatures of 800 and 1000 K, and at strain rates of 3500/s and 0.1/s. All the resulting microstructures have similar characteristics, that is, when the sample is deformed to a strain greater than 60%, the grains along the 45° angle to the loading direction, are seen to have elongated, and a broad deformation band is formed. This deformation band can further develop into an isothermal shearband with increasing strain. In contrast with the microstructure of the samples tested at temperatures 77 and 296 K, slip lines and second-phase precipitates disappear with increase temperature to 1000 K.

Summarizing the results of these microstructural characteristics of AL-6XN, we have actually observed material embrittlement with decreasing test temperatures to 77 K and high-strain rates. The ductility of this material increases markedly with increas-

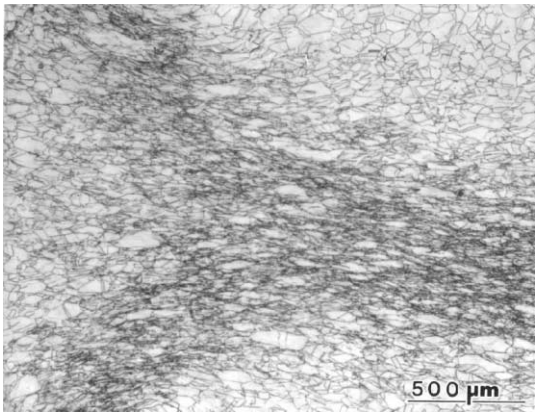

Fig. 10. Microstructure of a sample strained to $\gamma = 80\%$ at 1000 K and 0.001/s.

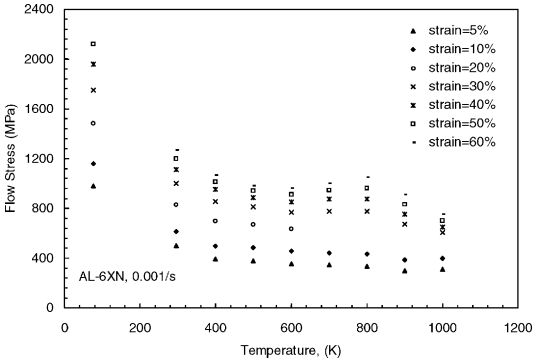

Fig. 11. Flow stress as a function of temperature for indicated strains and 0.001/s strain rate.

ing temperature. The embrittlement at low temperatures may be due to a structural transformation from austenite to martensite. In general, the temperature at which this transformation occurs is below room temperature, and depends on the alloying content and impurities in the material. The material, however, shows remarkable ductility over the entire considered temperature range.

2.3.2. Mechanical properties

From Fig. 2, we observe dynamic strain aging for test temperatures exceeding 500 K and a strain rate of 0.001/s, where the flow stress increases with increasing temperature. Using the data in Figs. 2–4, we have plotted the true stress vs. temperature in Fig. 11, for indicated strains. From this figure, dynamic strain aging is clearly displayed in the temperature range from 500 to 1000 K, with the maximum peak stress occurring at about 800 K. Dynamic strain aging increases with increasing strain. Fig. 12 shows

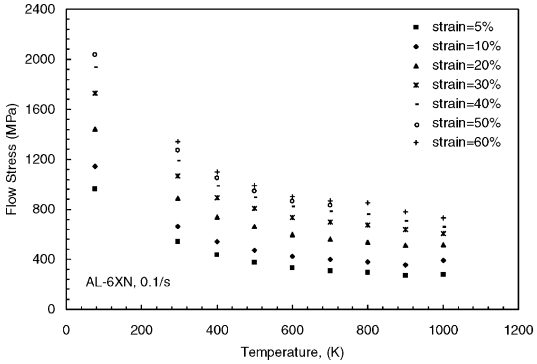

Fig. 12. Flow stress as a function of temperature for indicated strains and 0.1/s strain rate.

the flow stress as a function of temperature for indicated strains and a strain rate of 0.1/s. Comparing these results with those in Fig. 11, it is seen that the peak value of the flow stress in Fig. 12 is smaller than that in Fig. 11. This shows that the dynamic strain aging disappears with increasing strain rate, and that no dynamic strain aging is observed at a strain rate of 3500/s; see also Fig. 4.

From the data shown in Fig. 5, we note the remarkable difference between the isothermal and the adiabatic flow stress at a 77 K initial temperature. This difference is due to thermal softening which occurs in adiabatic tests at high strain rates. These experimental results quantify the temperature dependence of the material response. However, we have found that, as the temperature is increased to 500 K, the isothermal and adiabatic flow stresses are essentially the same. This response seems to deviate from the response of other metals (e.g., tantalum and molybdenum; Nemat-Nasser and Isaacs (1996) and Nemat-Nasser and Guo (1999)). Two questions need to be addressed: (1) is there any recovery during unloading and reloading which are necessary to obtain the isothermal flow stress; and (2) what are the temperature and strain rate effects on the flow stress? To answer these questions, we examine the relation between the flow stress and the temperature and strain rate, using several interrupted tests, involving both temperature and strain-rate jumps. These are discussed below.

2.3.2.1. Interrupted tests. To perform an interrupted test at a high-strain rate, the sample is heated or cooled to the required initial temperature in the furnace or liquid-nitrogen container attached to the recovery Hopkinson bar (Nemat-Nasser and Isaacs, 1996), and then reloaded at a pre-defined strain rate to a pre-defined strain. After each incremental loading, the sample is unloaded without being subjected to any additional stress pulses. Then the sample is allowed to return to room temperature, its dimensions measured, and it is reheated or recooled to the required temperature, and reloaded at the same strain rate. The interval between unloading and reloading is usually about 2–10 min, depending on the temperature of the sample. It is, therefore, necessary to check whether or not this process affects the microstructure of the material, and hence its subsequent response.

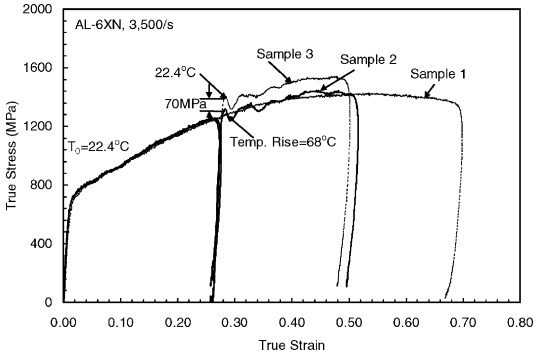

Fig. 13. Verification of heat conversion.

Three samples (designated as Samples 1, 2 and 3, respectively) are loaded at a same strain rate of 3500/s. Sample 1 is loaded to a true strain of about 68% at an initial temperature of 22.4°C (room temperature). The corresponding true stress–true strain curve is displayed by a dashed curve in Fig. 13. This is essentially an adiabatic true stress–true strain relation for the AL-6XN. The temperature rise in this adiabatic test is calculated using the following expression:

$$\Delta T = \int_0^{\lambda} \frac{\beta}{\rho' C_V} \tau \, \mathrm{d}\gamma, \tag{2.1}$$

where ρ' is the mass density (7.947 g/ccm), C_V is the temperature-dependent heat capacity (taken as 0.5 J/g K at room temperature; Russell et al., 1980), γ is the plastic strain, τ is the flow stress in MPa, and β is the fraction of the plastic work which is converted into heat. The value of β must be determined experimentally. Data reported by Kapoor and Nemat-Nasser (1998) for several metals suggest that, for large strains (e.g., $\gamma \geq 20\%$), β is essentially 1. This has also been verified to be the case for several bcc polycrystalline metals (see Nemat-Nasser et al., 1999a; Nemat-Nasser and Isaacs, 1996; and Nemat-Nasser and Guo, 1999). In the present case, $\beta \approx 1.0$ is also verified experimentally, as is shown in what follows.

Samples 2 and 3 are first loaded to a true strain of 26%, starting at the room temperature (22.4°C). Their true stress–strain relations are shown by thick solid curves in Fig. 13. These curves fall on the curve corresponding to Sample 1, showing the repeatability of the test results. The temperature rise at a true strain of 26% would be 68°C, when calculated using Eq. (2.1) with $\beta = 1.0$. In the absence of other effects, the stress–strain of Sample 2 when heated to 90.4°C (68 + 22.4) and reloaded at the same strain rate, should follow that of Sample 1. We have done this and the results are shown in Fig. 13 by the second thick solid curve. This curve follows closely the adiabatic curve of Sample 1, suggesting the validity of the assumptions, at least to within the present experimental accuracy. As a check, Sample 3 is reloaded at its initial room temperature (22.4°C), and the corresponding true stress–strain curve is displayed by the thin curve marked Sample 3. The stress difference between the adiabatic and this

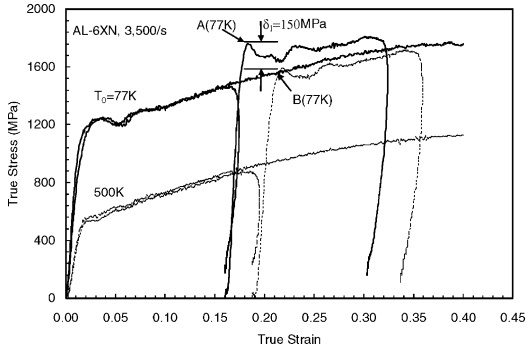

Fig. 14. Effect of temperature jump on flow stress from initial temperature 500 to 77 K.

isothermal curve is measured to be about 70 MPa, for a strain increment of 26%. It is clear that this stress difference (70 MPa) is due to only the temperature difference between the two samples. Two important conclusions are drawn from these results: (1) if there was any recovery between unloading and reloading, it did not affect the flow stress noticeably, as the interrupted curve of Sample 2 follows the uninterrupted curve of Sample 1; and (2) essentially the entire plastic work is converted to heat with a negligibly small amount being stored in the sample as the elastic energy of the dislocations and other defects.

2.3.2.2. Temperature effect on microstructural evolution. To check the temperature-history effect on the microstructural evolution of AL-6XN stainless steel, tests with temperature jumps are performed. In Fig. 14 two adiabatic stress–strain relations are given for a strain rate of 3500/s, one at a 77 K and the other at a 500 K initial temperature, respectively. These results are used as baselines to compare with the results obtained by interrupted tests at various temperatures, as discussed below. All these tests are at the same strain rate of 3500/s.

One sample is first strained to about 18% true strain, starting with an initial temperature of 500 K. This is shown by a thin curve in Fig. 14. The sample is then cooled to 77 K, and reloaded at 3500/s. These results are also displayed by a thin curve in Fig. 14. The corresponding yield stress is marked by B (77 K) in the figure.

Another sample is first strained to about 15% true strain at a 77 K initial temperature. This curve (heavy line) follows the baseline adiabatic curve at a 77 K initial temperature, as is seen in the figure. Then the sample is cooled to its initial temperature (77 K) and reloaded, attaining the yield stress marked by A (77 K) in the figure. The difference between points (yield stresses) A (77 K) and B (77 K) in Fig. 14, $\delta_1 = 150$ MPa, is due to the difference in the temperature histories of the two samples. A prior straining at an initial temperature of 500 K results in a lower yield stress when the sample is cooled to 77 K, as compared with a prior straining at an initial temperature of 77 K.

In Fig. 15 we have displayed the results of a temperature jump test from an initial 77 K to an initial 500 K. The two adiabatic curves are the same as in Fig. 14. But now, a

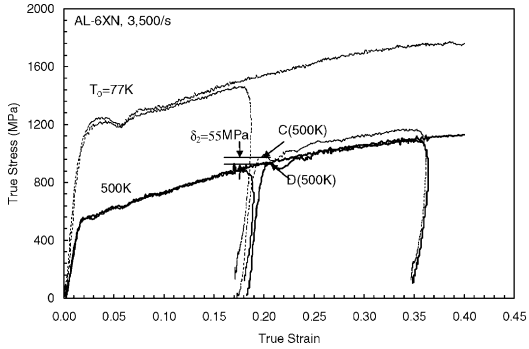

Fig. 15. Effect of temperature jump on flow stress from initial temperature 77 to 500 K.

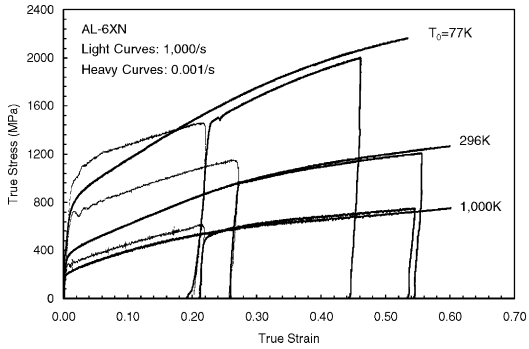

Fig. 16. Effect of strain-rate jump on flow stress from 1000 to 0.001/s.

sample is first deformed from an initial temperature of 77 K to about 17% true strain. It is then heated to 500 K and reloaded at a 3500/s strain rate. The corresponding yield point is marked C (500 K) in the figure. The two curves associated with this test are displayed by thin lines. Another sample is first loaded from an initial temperature of 500 K, unloaded, allowed to return to the same initial temperature of 500 K, and then reloaded, yielding at the point marked D (500 K) in the figure. As seen, the yield stress of the sample deformed at the lower temperature is now greater by 55 MPa than that which is first deformed at the higher temperature. Hence, the temperature history affects the microstructure and the response of this material.

2.3.2.3. Strain-rate effect on the microstructural evolution. It is commonly known that the strain-rate sensitivity of most materials increases rapidly with increasing strain rate (in general, $\geq$ 1000/s). In Fig. 16, the strain-rate effect on the flow stress of AL-6XN is examined by changing the strain rates from 1000/s to 0.001/s. In this figure, the heavy curves marked $T_0 = 77$, 296, and 1000 K are at a 0.001/s strain rate. These are the same as in Fig. 2. The light curves, on the other hand, represent the flow

stress at a strain rate of 1000/s and at the corresponding temperature of 77, 296, and 1000 K. It is seen that, even though the initial flow stress at a strain rate of 1000/s deviates from the corresponding curve at a 0.001/s strain rate, once the strain rate is changed from 1000/s to 0.001/s, the curves basically follow the associated heavy curves which are essentially the isothermal flow stresses at temperatures of 77, 296, and 1000 K. For the curves corresponding to 77 K, however, there is a difference of about 90 MPa, but the two curves are parallel.

Based on these results, we conclude that the strain rate and its history have a negligible effect on the microstructural evolution, as compared with that of the temperature history. The strain-rate effect disappears basically with increasing temperature. The difference in the flow stress for 1000/s and 0.001/s strain rates observed in Fig. 16 for strains less than 20%, possibly may be due to the drag on the motion of dislocations.

3. Physically based constitutive model

The experimental results reveal the following characteristics for AL-6XN stainless steel: (1) the plastic flow stress of this AL-6XN depends on the temperature, the strain rate, and their history (especially, temperature); (2) the dynamic strain aging occurs at low-strain rates and at the range of temperature from 500 to 1000 K, becoming weaker with increasing strain rates, or when the temperature exceeds 1000 K, but increasing with strain and attaining a peak value at about 800 K; (3) there is a viscous-drag resistance to the motion of dislocations, at a range of strain rates; and (4) the microstructure of the material evolves mainly with the temperature history.

A suitable constitutive model for this material should, therefore, include all the above effects. Based on the concept of dislocation kinetics, paralleled with a systematic experimental investigation, a physically based model is developed by Nemat-Nasser and co-workers (see, Nemat-Nasser and Isaacs, 1996; Nemat-Nasser and Li, 1998; Nemat-Nasser et al., 1999a, b; Nemat-Nasser and Guo, 1999) for several polycrystalline metals. A similar model which includes all the characteristics observed in AL-6XN stainless steel, does not exist. In the present work we seek to incorporate the experimental understanding presented above for AL-6XN, into the constitutive model suggested by Nemat-Nasser and co-workers. We will not, however, include the dynamic strain aging effects in the model.

We consider the plastic flow in the range of temperatures and strain rates where diffusion and creep are not dominant, and the deformation occurs basically by the motion of dislocations. We assume that the flow stress can be expressed as a combination of the thermal and athermal parts of the resistance to the dislocation motion. Here for the AL-6XN alloy, we assume that the flow stress, τ, consists of three parts: One part essentially due to the short-range thermally activated effect which may include the Peierls stress, point defects such as vacancies and self-interstitials, other dislocations which intersect the slip plane, alloying elements, and solute atoms (interstitial and substitutional). We denote this by τ^*. The second part is the athermal component, τ_a, mainly due to the long-range effects such as the stress field of dislocation forests and grain boundaries. Finally, a remaining viscous-drag component, τ_d, which

usually is important at high temperatures and high-strain rates. Thus, the flow stress is written as

$$\tau = \tau_a + \tau_d + \tau^*. \tag{3.1}$$

In this formulation, the total flow stress of a material, τ, is a function of the strain rate, $\dot{\gamma}$, temperature, T, and some internal microstructural parameters. The microstructure here refers to the grain sizes, the distribution of second-phase particles or precipitates, and the distribution and density of dislocations. In general, the most commonly used microstructural parameter is the average dislocation density, ρ. The microstructure can evolve differently for different loading conditions, that is, for different values of $\dot{\gamma}$ and T.

3.1. Athermal stress component, τ_a

The athermal part, τ_a, of the flow stress, τ, is independent of the strain rate, $\dot{\gamma}$. The temperature effect on τ_a is only through the temperature dependence of the elastic modulus, especially the shear modulus, $\mu(T)$ (Conrad, 1970). τ_a mainly depends on the microstructure of the material, e.g., the dislocation density, grain size, point defects, and various solute atoms such as those listed in Table 1. Based on linear elasticity, τ_a would be proportional to $\mu(T)$. Hence, we set

$$\tau_a = f(\rho, d_G, \ldots)\mu(T)/\mu_0, \tag{3.2}$$

where ρ is the average dislocation density, d_G is the average grain size, the dots stand for parameters associated with other impurities, and μ_0 is a reference value of the shear modulus. In a general loading, the strain γ represents the *effective* plastic strain which is a monotonically increasing quantity in plastic deformation. In the present case, γ defines the loading path and is also a monotonically increasing quantity, since $\dot{\gamma} > 0$. Therefore, it can be used as a load parameter to define the variation of the dislocation density, the average grain size, and other parameters which affect τ_a, i.e., we may set

$$\tau_a = f(\rho(\gamma), d_G(\gamma), \ldots)\mu(T)/\mu_0 = \hat{f}(\gamma)\mu(T)/\mu_0. \tag{3.3}$$

Further, as a first approximation, we may use a simple power-law representation of $\hat{f}(\gamma)$, and choose an average value for μ_0 so that $\mu(T)/\mu_0 \approx 1$. Then, τ_a may be written as

$$\tau_a \approx a_0 + a_1\gamma^n + \cdots, \tag{3.4}$$

where a_0, a_1, and n are free parameters which must be fixed experimentally.

3.2. Viscous-drag component, τ_d

Fig. 17 shows the flow stress vs. the strain rate for this AL-6XN, for indicated temperatures. It is seen that, the stress increases with increasing strain rate, especially when the strain rate exceeds about 1000/s. Fig. 18 displays the flow stress for 0.001/s, 0.1/s, and 3500/s strain rates, in terms of the temperature, for the same strain of 10%. From this figure, it is seen that the high-temperature flow stress at low strain

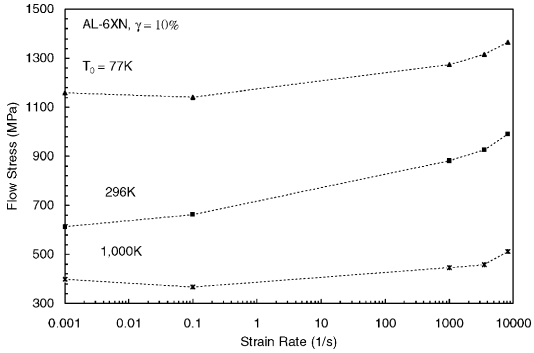

Fig. 17. Flow stress as a function of strain rate for indicated initial temperatures at 10% strain.

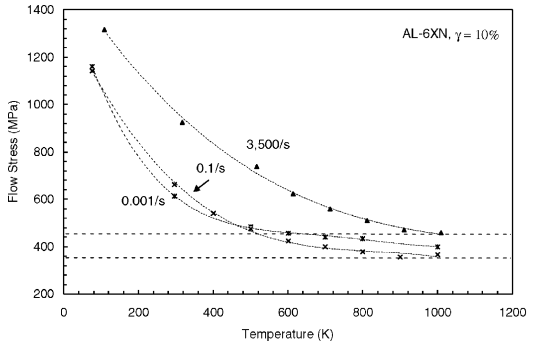

Fig. 18. Flow stress as a function of temperature for indicated strain rated and at 10% strain.

rates (0.001–0.1/s) is insensitive to the strain rate, but not at the high-strain rate of 3500/s. This increased strain-rate sensitivity is usually attributed to the electron- and phonon-drag effects on the mobile dislocations (see Follansbee and Weertman, 1982; Zerilli and Armstrong, 1992; Chiem, 1992; Regazzoni et al., 1987). The viscous-drag stress, τ_d, is usually related to the dislocation motion by $\tau_d \approx MBv/b$, where M is the Taylor factor, B is the drag coefficient, v is the average dislocation velocity, and b is the magnitude of the Burgers vector. Since v relates to the strain rate by $\dot{\gamma}=\rho_m bv/M$ (where ρ_m is the mobile dislocation density), it follows that $\tau_d \approx g(M^2B/(\rho_m b^2), \dot{\gamma}, T)$. At high temperatures, and in the absence of creep, the flow stress is essentially independent of the temperature, T, and we have

$$\tau_d \approx g(M^2B/(\rho_m b^2), \dot{\gamma}). \tag{3.5}$$

To examine the effect of the viscous drag on the flow stress of this AL-6XN, the results of Fig. 18 for a 1000 K temperature, are replotted in Fig. 19, including an additional point associated with the athermal stress for 8000/s. From these experimental results, it can be seen that, when the strain rate exceeds about 1000/s, the flow

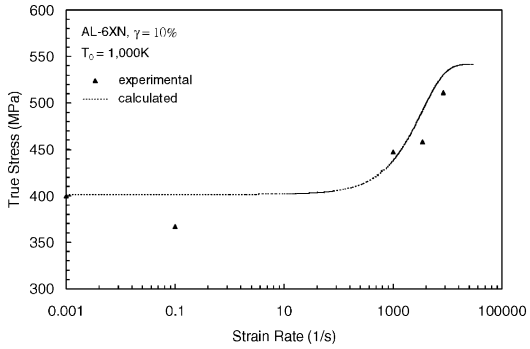

Fig. 19. High-temperature true stress as a function of strain rate for 1000 K initial temperature at 10% strain.

stress increases rapidly. Experimental results of Kapoor and Nemat-Nasser (1999) for tantalum show that the drag on dislocations is significant over a range of strain rates from a few hundred to several thousands per second. Based on this, we set

$$\tau_{\mathrm{d}} = m_0[1 - \exp(-\alpha\dot{\gamma})],$$

$$\alpha = \frac{M^2 B}{\rho_{\mathrm{m}} b^2 \tau_y}, \tag{3.6}$$

where m_0 is a material constant which can be measured directly at a very high-strain rate, and α represents an effective damping coefficient affecting the dislocation motion. Its value is fixed empirically. For the present case, we have obtained $\alpha \approx 3 \times 10^{-4}$ when $\dot{\gamma}$ is measured per second. This value of α corresponds to $M^2 \approx \mathrm{O}(10)$, $b = \mathrm{O}(10^{-10}\ \mathrm{m})$, $\rho_{\mathrm{m}} = \mathrm{O}(10^{13}/\mathrm{m}^2)$, and a high-temperature yield stress of $\tau_y = 140$ MPa, measured at a 1000 K temperature. Hence, the viscous-drag component of the flow stress, becomes

$$\tau_{\mathrm{d}} = 140[1 - \exp(-3 \times 10^{-4}\dot{\gamma})]. \tag{3.7}$$

3.3. Athermal- and drag- stress components of AL-6XN

To identify the constitutive parameters for the athermal stress in Eq. (3.4), we examine the variation of the flow stress with temperature, as shown in Figs. 11 and 12. These results suggest that the flow stress becomes essentially independent of the temperature, close to 1000 K and greater temperatures. These high-temperature values of the flow stress are plotted in Fig. 20, as stress versus the corresponding plastic strain. From Eqs. (3.4) and (3.7), the following final expression for the athermal and drag components of the flow stress, is obtained

$$\tau_{\mathrm{a}} + \tau_{\mathrm{d}} = 900\gamma^{0.35} + 140[1 - \exp(-3 \times 10^{-4}\dot{\gamma})]. \tag{3.8}$$

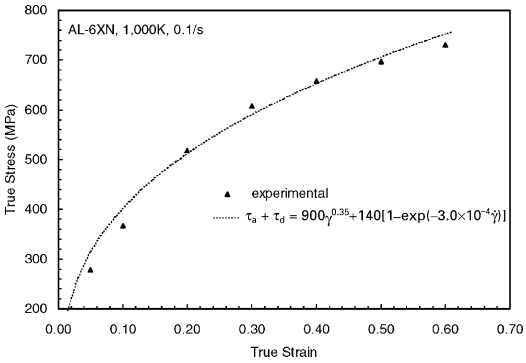

Fig. 20. Limiting values of flow stress as a function of strain at 1000 K and 0.1/s.

3.4. Thermally activated component of the flow stress, τ^*

The thermally activated flow stress, τ^*, in general, is a function of temperature, T, strain rate, $\dot{\gamma}$, and the internal variables characterizing the microstructure of the material. As discussed in connection with Figs. 14–16, the microstructure of this material evolves with the temperature history, but is not very sensitive to the strain rate. Consider the average dislocation density, ρ, as the most dominant microstructural parameter. Its evolution may be related to the (monotonically increasing) strain, γ; since $\dot{\gamma} > 0$, γ may be used as the loading parameter.

To obtain a relation between $\dot{\gamma}$, T, and τ^*, let ΔG be the activation free energy that a dislocation must overcome by its thermal energy. Kocks et al. (1975) suggest the following relation between ΔG and τ^*, representing a typical barrier encountered by a dislocation:

$$\Delta G = G_0 \left[1 - \left(\frac{\tau^*}{\hat{\tau}}\right)^p\right]^q,$$
$$G_0 = \hat{\tau} b \lambda \ell, \tag{3.9}$$

where $0 < p \leq 1$ and $0 \leq q \leq 1$ define the profile of the short-range barrier to the dislocation, $\hat{\tau}$ is the shear stress above which the barrier is crossed by a dislocation without any assistance from thermal activation, and G_0 is the free energy required for a dislocation to overcome the barrier solely by its thermal activation; λ and ℓ are the average effective barrier width and the dislocation spacing, respectively. We assume that $\dot{\gamma}$ is related to ΔG by

$$\dot{\gamma} = \dot{\gamma}_r \exp\left(-\frac{\Delta G}{kT}\right), \tag{3.10}$$

where $\dot{\gamma}_r = \rho_m b\bar{v}$; here, k is the Boltzmann constant, and $\bar{v} = \omega_0 \ell$ is the average velocity of the mobile dislocations, where ω_0 is the attempt frequency. From Eqs. (3.9)

and (3.10), obtain

$$\tau^* = \hat{\tau}\left[1 - \left(-\frac{kT}{G_0}\ln\frac{\dot{\gamma}}{\dot{\gamma}_r}\right)^{1/q}\right]^{1/p}. \tag{3.11}$$

To account for the microstructural evolution which affects the average dislocation spacing, ℓ, Nemat-Nasser and Li (1998) have assumed that $\ell = \ell_0 f(\gamma, T)$, where ℓ_0 is a reference (e.g., initial) average dislocation spacing. In view of Eqs. (3.9)–(3.11), this gives

$$\hat{\tau} = \tau^0 f(\gamma, T) \quad \text{and} \quad \dot{\gamma}_r = \frac{\dot{\gamma}_0}{f(\gamma, T)},$$
$$\tau^0 = \frac{G_0}{b\lambda\ell_0}, \quad \dot{\gamma}_0 = \rho_m b\omega_0\ell_0. \tag{3.12}$$

It is reasonable to expect that the average dislocation density increases with straining (work hardening) and that it decreases with increasing temperature (annealing). Based on this observation, and guided by our experimental results, we follow Nemat-Nasser and Li (1998) and assume that

$$f(\gamma, T) = \frac{\ell_0}{\ell} = 1 + a\left[1 - \left(\frac{T}{T_m}\right)^2\right]\gamma^m, \tag{3.13}$$

where a is a free parameter and depends on the initial average dislocation (the higher the initial dislocation density, the smaller is a), T_m is the melting temperature (approximately 1673 K), and the index m is a free parameter which must be evaluated from the experimental data. Combining Eqs. (3.11) and (3.13), we arrive at the following expression for τ^*:

$$\tau^* = \tau^0\left\{1 - \left[-\frac{kT}{G_0}\ln\frac{\dot{\gamma}\cdot f(\gamma, T)}{\dot{\gamma}_0}\right]^{1/q}\right\}^{1/p} f(\gamma, T) \quad \text{for } T \le T_c,$$
$$\tau^0 = \frac{G_0}{b\lambda\ell_0}, \quad \dot{\gamma}_0 = b\rho_m\omega_0\ell_0, \quad f(\gamma, T) = 1 + a\left[1 - \left(\frac{T}{T_m}\right)^2\right]\gamma^m, \tag{3.14}$$

where T_c is given by

$$T_c = -\frac{G_0}{k}\left(\ln\frac{\dot{\gamma}\cdot f(\gamma, T_c)}{\dot{\gamma}_0}\right)^{-1}. \tag{3.15}$$

Note that $\tau^* = 0$ for $T > T_c$.

In Eq. (3.14), the parameters p and q define the profile of the short-range energy barrier to the motion of dislocations. Ono (1968) and Kocks et al. (1975) suggest that $p = \frac{2}{3}$ and $q = 2$ are suitable values for these parameters for many metals. Nemat-Nasser and co-workers (1996, 1998, 1999) have verified this suggestion for several metals. Here, for AL-6XN, we use the same values for p and q in Eq. (3.14). The parameters k/G_0 and $\dot{\gamma}_0$ define the temperature and strain-rate dependency of the materials. Greater temperature sensitivity is associated with larger k/G_0, whereas larger $\dot{\gamma}_0$ corresponds to a smaller strain-rate sensitivity. The product $(k/G_0)/\ln(\frac{\dot{\gamma}}{\dot{\gamma}_0})$ can be estimated directly

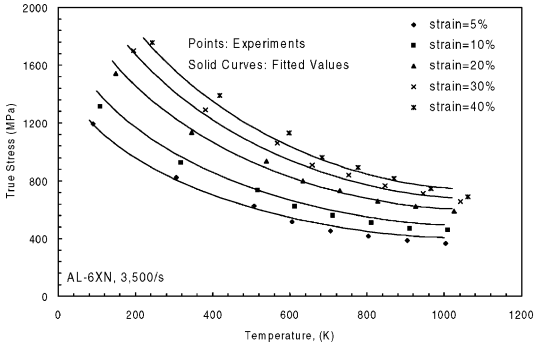

Fig. 21. Comparison between experimental results and modeling at indicated strains.

from the experimental data of Fig. 21. We have found that $k/G_0 \approx 6.6 \times 10^{-5}\ \mathrm{K}^{-1}$ and $\dot{\gamma}_0 \approx 2 \times 10^{10}/\mathrm{s}$ are suitable values in the present case. The first corresponds to an energy barrier of about 2 eV, and the second can be estimated by setting $b = \mathrm{O}(10^{-10}\ \mathrm{m})$, $\omega_0 = \mathrm{O}(10^{12}/\mathrm{s})$, $\rho_{\mathrm{m}} = \mathrm{O}(10^{13}/\mathrm{m}^2)$ and $\ell_0 = \mathrm{O}(10^3)$ lattice spacing. For the other parameters, we choose $m = \frac{1}{2}$ which correctly relates γ to the dislocation density, and set $a = 5$. Finally, we fix τ^0 empirically at $\tau^0 = 630$ MPa which also has the correct order of magnitude, based on $\tau^0 = G_0/(b\lambda\ell_0)$, with $\lambda = \mathrm{O}(10^{-10}\ \mathrm{m})$.

Now, the final constitutive relation for this material becomes, for $T \leq T_{\mathrm{c}}$,

$$\tau = 900\gamma^{0.35} + 140[1 - \exp(-3 \times 10^{-4})] + 630\left\{1 - \left[-6.6 \times 10^{-5} T \ln \frac{\dot{\gamma} f(\gamma, T)}{2 \times 10^{10}}\right]^{1/q}\right\}^{1/p} f(\gamma, T), \tag{3.16}$$

where

$$T = T_0 + 0.25 \int_0^{\gamma} \tau \, \mathrm{d}\gamma, \quad f(\gamma, T) = 1 + 5\left[1 - \left(\frac{T}{1673}\right)^2\right]\gamma^{1/2},$$

and for $T > T_{\mathrm{c}}$, we have

$$\tau = 900\gamma^{0.35} + 140[1 - \exp(-3 \times 10^{-4}\dot{\gamma})], \tag{3.17}$$

where,

$$T_{\mathrm{c}} = -6.6 \times 10^{-5}\left[\ln \frac{\dot{\gamma} f(\gamma, T_{\mathrm{c}})}{2 \times 10^{10}}\right]^{-1}.$$

Figs. 22–25 compare the experimental results with the model predictions at the high-strain rates of 1000/s and 3500/s, for indicated initial temperatures. To further verify the model, independent tests at an 8300/s strain rate and various initial temperatures are performed, and the results are displayed in Fig. 26. As seen, good correlation between these data and the model predications, is obtained.

As pointed out before, the model does not include the dynamic strain aging effects, which occur in the temperature range of 500–1000 K, at the low strain rates of 0.001/s

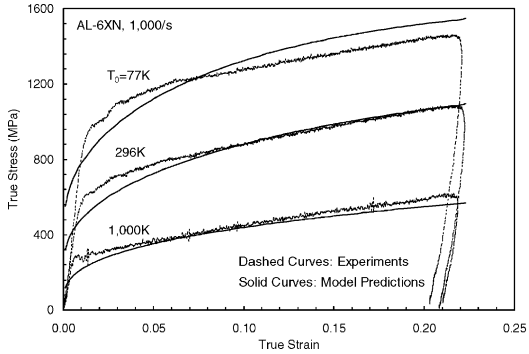

Fig. 22. Comparison of model predictions with experimental results at a strain rate of 1000/s.

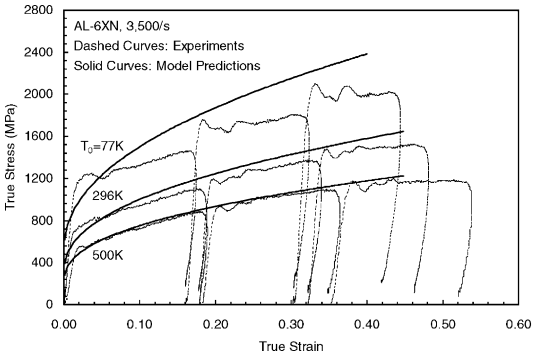

Fig. 23. Comparison of model predictions with experimental results at a strain rate of 3500/s.

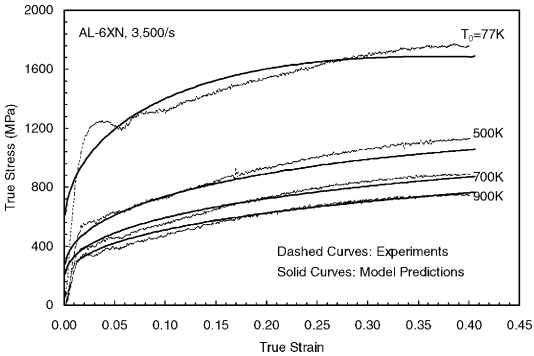

Fig. 24. Comparison of model predictions with experimental results at a strain rate of 3500/s.

and 0.1/s. In Figs. 27 and 28 we have shown the experimental results for these low strain rates. Besides the effect of dynamic strain aging, the model predictions are in reasonable agreement with the experimental results.

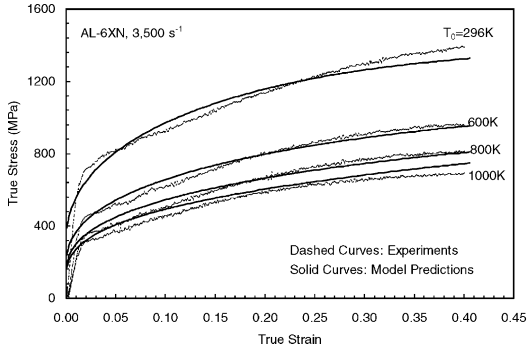

Fig. 25. Comparison of model predictions with experimental results at a strain rate of 3500/s.

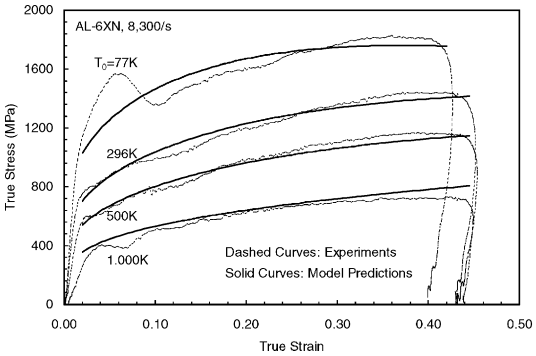

Fig. 26. Comparison of model predictions with experimental results at a strain rate of 8000/s.

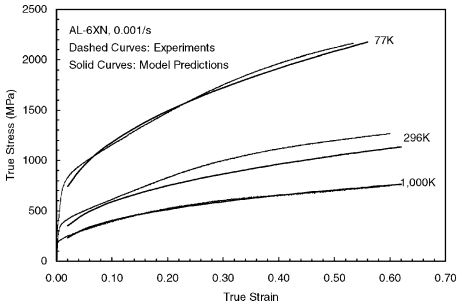

Fig. 27. Comparison of model predictions with experimental results at a strain rate of 0.001/s.

4. Conclusions

Uniaxial compression tests of cylindrical samples are performed to investigate the flow stress behavior of AL-6XN austenitic stainless steel. Strains exceeding 40% are achieved in these tests, over a range of strain rates from 0.001/s to about 8000/s, and

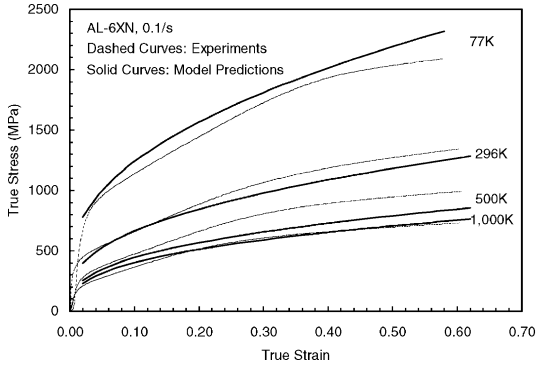

Fig. 28. Comparison of model predictions with experimental results at a strain rate of 0.1/s.

at temperatures from 77 to 1000 K. In an effort to understand the underlying deformation mechanisms, some interrupted tests with temperature and strain rate jumps are also performed. The microstructure of undeformed and deformed samples is examined. Several noteworthy conclusions are as follows:

1. At low temperatures and high-strain rates, adiabatic shearbands form if the strain exceeds about 40%, leading to failure upon further straining.
2. AL-6XN stainless steel displays good ductility (strain $> 40\%$) at low temperatures and high-strain rates, with its ductility increasing with temperature.
3. Dynamic strain aging occurs within a temperature range of 500–1000 K at lower strain rates, becoming more pronounced with increasing strain. The maximum peak value of the stress in dynamic strain aging, occurs at about an 800 K temperature for 0.001/s and 0.1/s strain rates.
4. The temperature has a greater effect on the flow stress of AL-6XN than does the strain rate.
5. Based on the experimental results, taking into account the viscous-drag effect, a physically based model is developed. In the absence of dynamic strain aging, the model predictions are in good agreement with the experimental results over a wide range of temperatures and strain rates.

Acknowledgements

The authors would like to thank Mr. Jon Isaacs for his assistance in preparing samples, and Dr. Ning Wang for his help in examining the microstructure of the material. This work has been supported, in part, by ONR Contract, N00014-96-1-0631, to the University of California, San Diego.

References

Brooks, J.A., Lippold, J.C., 1990. Selection of wrought austenitic stainless steels. ASM Handbook. ASM International, Vol. 6, pp. 457–469.

Conrad, H., 1970. The athermal component of the flow stress in crystalline solids. Mater. Sci. Engng. 6, 260–264.

Chiem, C.Y., 1992. Material deformation at high strain rates. In: Meyers, M., Murr, L., Staudhammer, K (Eds.), Shock-Wave and High-Strain-Rate Phenomena in Materials. Marcel Dekker, New York, pp. 69–85.

Denhard, E.E., Espy, R.H., 1972. Austenitic stainless steels with unusual mechanical and corrosion properties. Met. Engng. Quart. 18–20.

Follansbee, P.S., Weertman, J., 1982. On the question of flow stress at high strain rates controlled by dislocation viscous flow. Mech. Mater. 1, 345–350.

Gaugh, R.R., Perry, D.C., 1972. A new stainless steel for the CPI. Chem. Engng. Magazine, October, McGraw Hill, pp. 84–90.

Hecker, S.S., Stout, M.G., Staudhammer, K.P., Smith, J.L., 1982. Effects of strain state and strain rate on deformation induced transformation in 304 stainless steel. I. Magnetic measurements and mechanical behavior. Metall. Trans. A 13A, 619–626.

Horii, H., Nemat-Nasser, S., 1985. Elastic fields of interacting inhomogeneities. Int. J. Solids Struct. 21, 731–745.

Horii, H., Nemat-Nasser, S., 1986. Brittle failure in compression splitting, faulting and brittle–ductile transition. Philos. Trans. Roy. Soc. London A 319, 337–374.

Ishikawa, K., Tanimura, S., 1992. Strain rate sensitivity of flow stress at low temperatures in 304N stainless steel. Inter. J. Plasticity 8, 947–958.

Kapoor, R., Nemat-Nasser, S., 1998. Determination of temperature rise during high strain rate deformation. Mech. Mater. 27, 1–12.

Kapoor, R., Nemat-Nasser, S., 1999. Comparison between high strain-rate and low strain-rate deformation of tantalum. Metall. & Mater. Trans. 31A, 815–823.

Kocks, U.F., Argon, A.S., Ashby, M.F., 1975. Thermodynamics and kinetics of slip. Prog. Mater. Sci. 19, 1–271.

Liao, S.C., Duffy, J., 1998. Adiabatic shear bands in a Ti–6Al–4V titanium alloy. J. Mech. Phys. Solids 46, 2201–2231.

Merzer, A.M., 1982. Modeling of adiabatic shear band development from imperfections. J. Mech. Phys. Solids 30, 323–338.

Nemat-Nasser, S., Guo, W.G., 1999. Flow stress of a commercially pure niobium and its model. Mater. Sci. Engng. A 284, 202–210.

Nemat-Nasser, S., Guo, W.G., Cheng, J.Y., 1999b. Mechanical properties and deformation mechanisms of a commercially pure titanium. Acta Mater. 47, 3705–3721.

Nemat-Nasser, S., Guo, W.G., Liu, M.Q., 1999a. Experimentally based micromechanical modeling of dynamic response of molybdenum. Scripta Mater. 40, 859–872.

Nemat-Nasser, S., Horii, H., 1982. Compression-induced nonplanar crack extension with application to splitting, exfoliation and rockburst. J. Geophys. Res. 87, 6805–6821.

Nemat-Nasser, S., Isaacs, J.B., 1996. Direct measurement of isothermal flow stress of metals at elevated temperatures and high strain rates with application to Ta and Ta–W alloys. Acta Mater. 45, 907–919.

Nemat-Nasser, S., Isaacs, J.B., Starrett, J.E., 1991. Hopkinson techniques for dynamic recovery experiments. Proc. Roy. Soc. London 435 (A), 371–391.

Nemat-Nasser, S., Li, Y.L., 1998. Flow stress of fcc polycrystals with application to OFHC Cu. Acta Mater. 46, 565–577.

Ono, K., 1968. Temperature dependence of dispersed barrier hardening. J. Appl. Phys. 39, 1803–1806.

Regazzoni, G., Kocks, U.F., Follansbee, P.S., 1987. Dislocation kinetics at high strain rates. Acta Metall. 35, 2865–2875.

Russell, B.G., et al. (ASM committee on wrought stainless steels), 1980. Wrought stainless steels. ASM Metals Handbook, 9th Edition, Vol. 3, pp. 3–40.

Stout, M.G., Follansbee, P.S., 1986. Strain rate sensitivity, strain hardening, and yield behavior of 304L stainless steel. Trans. ASME, J. Engng. Mater. Technol. 108, 344–353.

Wu, F.H., Freund, L.B., 1984. Deformation trapping due to thermoplastic instability in one-dimensional wave propagation. J. Mech. Phys. Solids 32, 119–132.

Zerilli, F.J., Armstrong, R.W., 1992. The effect of dislocation drag on the stress–strain behavior of fcc metals. Acta Metall. Mater. 40, 1803–1808.